IOP Publishing | International Atomic Energy Agency Nuclear Fusion

Nucl. Fusion **61** (2021) 076001 (10pp) https://doi.org/10.1088/1741-4326/abf952

Material migration in W and Mo during bubble growth and fuzz formation

M.I. Patino[1,*], D. Nishijima[1], M. Tokitani[2], D. Nagata[1,2], J.H. Yu[1] and R.P. Doerner[1]

[1] Center for Energy Research, University of California at San Diego, La Jolla, CA 92093-0417, United States of America
[2] National Institute for Fusion Science, Toki, Gifu, Japan

E-mail: m2patino@ucsd.edu

Received 16 February 2021, revised 8 April 2021
Accepted for publication 19 April 2021
Published 13 May 2021

Abstract

Growth of helium (He) induced bubbles and fuzz in tungsten (W) and molybdenum (Mo) is investigated using samples of W films on Mo substrates and Mo films on W substrates exposed to He-containing plasma in the temperature range of 340 to 1075 K, fluence range of 1.0–14 $\times$ 10^{25} He·m^{-2}, and incident ion energy of <50 eV. No fuzz (only up to 2 nm diameter bubbles) and no material transport occur in W films at $\leqslant$750 K, while precursors-of or fully-developed fuzz and material mixing occur in W and Mo films at $\geqslant$800 K. This suggests that fuzz forms in multi-material systems as long as one material meets the conditions for fuzz formation, namely $T_s/T_m \sim 0.27$–0.5 where T_s and T_m are the sample exposure and material melting temperatures, respectively. Larger He bubbles, more material mixing, and further-developed fuzz occur at higher temperature due to increased mobility of He atoms and small He clusters. Accumulation of substrate material at the surface of fuzzy W and Mo thin-film (<80 nm) samples suggests fuzz growth by material transport from the bubble layer in the bulk up to the fiber tip, likely by a two-step process: (i) diffusion of punched dislocation loops in the bulk toward the fuzz base and (ii) diffusion of adatoms along the fuzz base and fiber surface (with effective transport of adatoms upwards due to trapping of adatoms at curved surfaces of fiber tips and/or due to the continuous generation of adatoms at the fuzz base). While the bubble size and fuzz thickness increase with reduced W concentration in Mo thin-film samples at 838 K likely due to an increase in trap mutation and dislocation loop punching in Mo compared to W, the fuzz thickness decreases with reduced W concentration at 1075 K despite an increase in the bubble size likely due to slower diffusion of interstitial loops in Mo.

Keywords: bubbles, fuzz, helium, tungsten, molybdenum, plasma-material interactions

(Some figures may appear in colour only in the online journal)

1. Introduction

Tungsten (W) has been chosen for the divertor region of ITER due to its favorable thermo-mechanical properties and low hydrogen-isotope retention. Yet, W has been shown in linear plasma devices and magnetic confinement facilities to develop nano-sized bubbles and fuzz when exposed to helium (He) ions that can adversely affect bulk W properties [1–5]. Conditions for W fuzz formation (sample temperature $T_s \sim 1000$–2000 K [6], He ion energy $E_i \geqslant 20$–30 eV [6, 7], and He ion fluence $\Phi_{He} \geqslant 2.5 \times 10^{24}$ m^{-2} [8, 9]) are expected to be met at the divertor outer vertical target in ITER, and up to μm-thick fuzz may develop during D-T operation without edge localized modes (ELMs) or with low energy ELMs [10–12].

He bubbles (precursors to fuzz) form by the following process: (i) implantation of He ions into W; (ii) diffusion of He

* Author to whom any correspondence should be addressed.

atoms in the bulk and trapping at other He atoms, defects, and impurities to form clusters; (iii) growth of He clusters to form bubbles via trap mutation when the pressure of He clusters exceeds a critical value, whereby vacancy-interstitial pairs are created, vacancies are incorporated into the expanding bubble to relieve pressure, and W interstitials are bound in close proximity to the bubble; and (iv) growth of He bubbles via punching of W interstitial loops around bubbles when the He bubble pressure exceeds another critical value [13 and the references therein, 14]. The pressure thresholds for trap mutation and loop punching are $p \geqslant 2\gamma/r + \mu/2$ and $p \geqslant 2\gamma/r + \mu b/r$, respectively, where μ, b, γ, and r are material shear modulus, length of the Burger's vector, surface free energy, and radius of the cluster/bubble [15].

Multiple theories for fuzz growth have been suggested, including diffusion of dislocation loops to the W surface [13, 16]. Other fuzz formation theories include (i) bubble bursting and the creation of deep trenches as bubbles continually intersect the surface [6], (ii) tensile stress-driven fracturing of material around He bubbles to form fuzz fibers [17] (iii) migration of ion-induced adatoms along the fiber surface from the base to the tip [18, 19], (iv) viscoelastic flow of material to the tip around bubbles within individual fibers [20], and (v) the extraction of material upwards due to the sheath electric field [21]. While fuzz growth due to electric field effects has been disproven by reference [22] in experiments whereby W pre-irradiated with He plasma showed no further fuzz formation with sequential hydrogen or neon plasma, the exact mechanism of fuzz formation is still not resolved.

Previously we investigated the transport of near-surface W and Mo atoms during fuzz formation using molybdenum (Mo) thin (∼45 nm) films deposited on W substrates and exposed to He plasma at T_s = 838–1075 K, $\Phi_{He} = 3.4 \times 10^{25}$ m^{-2}, and $E_i < 40$ eV [23]. We found that the developed fuzz contained both Mo and W at all temperatures, with the fuzz thickness (and size of surrounding bubbles) increasing with temperature. Here we present additional experiments whereby the dependence of material transport on Mo film thickness is explored. Data from reference [23] is reproduced here for completeness. Samples using thin Mo coatings on W are denoted as 'Mo–W'. Furthermore, we investigate material transport using W thin films on Mo substrates at a larger range of exposure temperatures including temperatures below which only He bubbles and not fuzz are formed. Samples using thin W coatings on Mo substrates are denoted as 'W–Mo'.

Experiments utilized polycrystalline substrates that were polished to a mirror finish and coated with thin metal films via magnetron sputtering deposition. Plasma exposures were carried out in the PISCES-A linear plasma device [24]. Incident ion energies, E_i, were controlled by negatively biasing the sample, and plasma properties including ion flux, Γ_i, were measured with a fast reciprocating Langmuir probe. The sample temperature, T_s, was measured by a thermocouple pressed against the backside of the sample and controlled by varying the forced air through the sample holder. Experimental approaches and results examining the dependence of nanostructure formation and material migration on T_s and film thickness, t_{film}, are discussed in sections 2 and 3, respectively. Section 4 summarizes results.

2. Temperature dependence (W film on Mo)

The transport of near-surface W and Mo atoms during He bubble growth and fuzz formation was examined in a temperature dependence study. 35–59 nm thick W films were deposited on polished Mo substrates as determined from mass gain measured with a microbalance. Samples were subsequently exposed to He plasma at T_s between 340 and 1000 K, $E_i \sim$ 45 eV, and $\Phi_{He} \geqslant 1.0 \times 10^{25}$ m^{-2}. Plasma exposure conditions for the seven samples (i.e. W–Mo 4–6 and W–Mo 10–13) are summarized in table 1. An additional sample, W–Mo 14, was exposed to pure D plasma at similar conditions. Slight erosion was detected from mass loss measurements, likely from impurities in the plasma, resulting in calculated film thicknesses indicated in figure 1.

After plasma exposure, surface topography was examined with scanning electron microscopy (SEM) using a ThermoFisher Scientific Apreo. Cross-sectional views were obtained with a transmission electron microscope (TEM) after preparing thinned samples with a focused ion beam. Elemental composition maps of the thinned samples were obtained with energy dispersive x-ray (EDX) spectroscopy. The elemental composition was also determined with Auger electron spectroscopy (AES) in a PHI 590; only Mo and W, not residual carbon and oxygen, are considered here. Measurements were made at multiple locations on the sample surface. Profiles of the composition as a function of depth were made by alternating cycles of sputtering with 4 keV Ar ions and AES measurement with 3 keV electrons. Note that while the mean free path of incident ions is larger in fuzz than in smooth material due to fuzz porosity, material sputtered from fuzz is redeposited on neighboring fuzz fibers [25], resulting in a reduced sputter rate. The mean free path of incident and emitted electrons is likewise larger in fuzz than smooth material, yet emitted electrons are recollected on fuzz fibers [26], resulting in AES information being collected from depths larger than 3 nm but much smaller than the fuzz thickness. The AES depth profiles of fuzzy samples should be carefully considered as these effects were not considered in the depth calibration.

Figure 2 shows SEM images of the top view of all samples. As can be seen, no fuzz is observed on the surface of samples exposed at ⩽750 K. In figure 1(*a*), no Mo is observed in the AES depth profiles until depths matching the film thickness of the samples, including for the edge region covered during plasma exposure by the sample-holding cap. Hence a lack of transport of Mo from the substrate into the W film is demonstrated. This is confirmed by the EDX map of W–Mo 11 (700 K), with ∼0% Mo measured in the region within the blue box in figure 3(*a*). Thus, a lack of both fuzz formation and material mixing occurs at these low temperatures. Yet, He bubbles up to 2 nm in diameter are observed in the zoomed-in TEM image of W–Mo 11 in figure 3(*a*), where bubbles are mainly located in the film.

As seen in figure 1(*b*), Mo from the substrate is first observed on the surface of W–Mo 10 which was exposed at

Table 1. Plasma exposure conditions for W thin films on Mo substrates. Surface features and concentrations of Mo after plasma exposure are also included.

Sample	T_s (K)	t_{film} (nm)	E_i (eV)Γ_i (10^{21} m^{-2} s^{-1})	Φ_{He} (10^{25} m^{-2})	Surface features	Surface Mo (at%)
W–Mo 5	340	56 ± 10	43	0.6–1.4	1.0	None	0
W–Mo 4	565	59 ± 5	45	2–4	1.0	None	0
W–Mo 11	700	46 ± 4	47	5–7	1.0	None	0
W–Mo 12	750	45 ± 3	49	6–10	1.2	None	0
W–Mo 10	800	35 ± 3	47	10–15	1.4	Pinholes	19–23
W–Mo 13	800	41 ± 3	49	9–17	14	Pinholes	16–22
W–Mo 6	1000	58 ± 5	47	8–9	1.0	275 nm fuzz	46–60
W–Mo 14	800	39 ± 5	74	6 (D)	1.1 (D)	<10 μm blisters	0

800 K. Up to 50 nm diameter pinholes are also observed on the surface of W–Mo 10 (see figure 2(*e*)), and are thought to be precursors for fuzz. As the fluence is increased from 1.4×10^{25} to 1.4×10^{26} m^{-2} (i.e. W–Mo 13) at the same $T_s \sim 800$ K, the size of pinholes at the surface increases. Similar Mo concentrations (16%–23%) are observed at the surface of W–Mo 10 and 13, yet more Mo is observed at depths of 20–85 nm in figure 1(*b*) at the higher fluence. A lack of material mixing at the unexposed edge (which experienced the same heat treatment as W–Mo 10 but no incident He), demonstrates that thermal diffusion does not occur.

While the implantation depth of 50 eV He^+ in W is <2 nm [27], He atoms may diffuse and reach the Mo substrate. From reference [28], fuzz grows on pure Mo at >770 K and $\geqslant 8.6 \times 10^{24}$ He·m^{-2}. However, fuzz grows on pure W at $\geqslant$1000 K [6]. Therefore, the existence of W in the fuzz precursor at 800 K as determined from the AES depth profile in figure 1(*b*) is unexpected. Yet fuzz made of W (62% W, 31% Fe, and 7% Cr) was also observed (superimposed on cone structures) after reduced-activation ferritic/martensitic steel was exposed to He plasma at temperatures down to 773 K [29, 30]. Fuzz forms on pure Fe at 800 K [31], while no fuzz forms on pure Cr. Therefore, results here and in the literature suggest that fuzz forms in materials if conditions are met for one component to form fuzz, and other components that do not generally meet the conditions for fuzz formation may still be incorporated into the fuzz.

W–Mo 14 was exposed to pure D plasma, instead of He, at conditions similar to W–Mo 10 (800 K, 1.1×10^{25} m^{-2}). No pinholes (only blisters up to 10 μm in diameter) were observed on the surface in figure 2(*h*). In addition, the Mo depth profile in figure 1(*b*) shows no Mo transport during D plasma exposure, suggesting Mo transport in He-exposed samples at high temperature is associated with the nanostructure formation and not due to thermal diffusion.

Fully developed fuzz was observed on W–Mo 6, which was exposed at 1000 K (see figure 2(*g*)). The fuzz thickness and fiber diameter were measured with SEM and TEM to be 275 ± 80 nm and 20–110 nm, respectively. Significant Mo was detected in the fuzzy layer with an accumulation of the Mo substrate at the top and a decrease toward the fuzz base: 60 and 42% Mo were measured by AES at the surface and at ~200 nm, respectively, in figure 1(*c*), while 76 and 27% Mo were measured by EDX in the top and bottom blue boxes in figure 3(*b*). Similar accumulation of substrate material at the surface within the uppermost ~50 nm was observed by reference [32] when exposing a 15 nm ^{182}W-rich film on W substrate with natural isotopic distribution to He plasma at 1100 K to form fuzz. As discussed in reference [23], accumulation of the substrate material at the fuzz tip suggests material migration upwards and fuzz growth from the fuzz tip outwards. Fuzz growth from the surface outwards was also observed by references [33, 34] when comparing the height measured by cross-sectional SEM of the fuzzy-exposed and smooth-unexposed regions. However, this disagrees with work by reference [35] where fuzz growth from the fuzz base upwards was assumed from grain boundary misorientation histograms (similar among tendril/tendril and substrate/tendril grain boundaries). Reference [22] also assumed fuzz growth from the base upwards from W–Mo thin films experiments similar to those presented here, but used AES depth profiles with depth resolution insufficient to capture the substrate accumulation at the surface.

As mentioned in section 1, the theory for fuzz growth by extraction of material upwards by the sheath electric field [21] was invalidated by reference [22] in experiments whereby W pre-irradiated with He plasma showed no further fuzz formation with sequential hydrogen or neon plasma, despite maintaining similar plasma conditions. Pinholes observed during *initial* fuzz formation in figures 2(*a*) and (*b*) (and by many other groups) may be explained by He bubbles intersecting the surface. However, continuous creation of deep trenches by He bubbles pushing up the surface and intersecting the surface [6, 8] would not lead to substrate material accumulation at the surface as observed here and in reference [32], suggesting this theory for *continual* fuzz formation is not valid. Fan *et al* [17] suggested fuzz growth by enlargement of pinholes at the surface, with material loops formed around pinholes at step edges or protrusions which get thinner with He fluence and fracture due to bubble-induced tensile stress, resulting in the formation of three dimensional fibers. While it may explain *initial* fuzz growth, it too would not result in substrate accumulation at the fuzz surface observed during *continual* fuzz growth.

Instead, substrate accumulation at the fuzz surface and fuzz growth from the tip by material migration upwards is thought to occur when interstitial dislocation loops created during bubble growth/trap mutation are punched and when these diffuse from the bulk toward the surface at the fuzz base, becoming adatoms [13, 16]; note that incident He was previously found

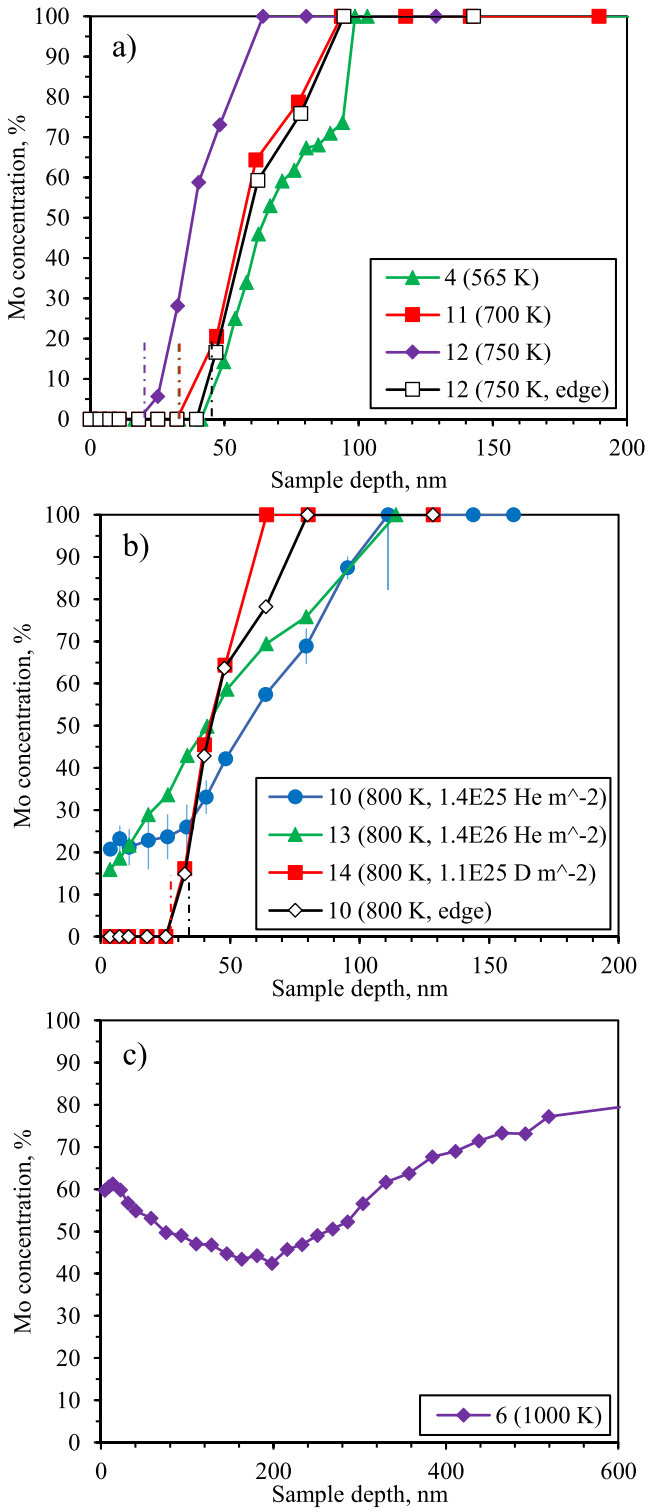

Figure 1. Concentration of Mo as a function of depth for thin W films on Mo substrates after exposure to pure He plasma at ~45 eV, 1.0–1.4 × 10^{25} m^{-2}, and (*a*) 565–750 K, (*b*) 800 K, or (*c*) 1000 K. Also included in (*b*) are profiles for samples exposed at 800 K to 1.4 × 10^{26} He·m^{-2} and 1.1 × 10^{25} D·m^{-2}. Dashed lines along the abscissa in (*a*) and (*b*) indicate film thicknesses at exposed and unexposed regions. (Note that the sample depth calibration does not consider differences in sputtering rate and AES information depth for fuzzy samples.)

to be capable of penetrating an up to 3 μm thick fuzz layer to reach the bulk [32]. Adatoms with sufficient thermal energy to overcome the activation energy can then diffuse randomly up and down along the fiber surface but trap at curved surfaces, including at the tip of individual fuzz fibers due to the higher binding energy [19], resulting in an effective adatom diffusion upwards. Diffusion of adatoms from regions of high adatom concentration (i.e. the fuzz base where punched dislocation loops generate a continuous source of adatoms during plasma exposure) to regions of low adatom concentration (i.e. the fuzz tip) may also result in their effective transport upwards. At low He fluence, the bubble region lies within the W film and W interstitial loops and adatoms are generated, resulting in fuzz made of W. At high fluence, the region reaches the Mo substrate, Mo interstitial loops are generated, and Mo adatoms are expected to reach the top of fuzz fibers. In fact, for W–Mo 6 with He fluence = 1.0 × 10^{25} m^{-2}, the fiber tip is comprised of atoms primarily (i.e. ~60%–80%) from the Mo substrate that have migrated outwards. The Mo concentration map of sample W–Mo 6 in figure 3(*b*) clearly shows that Mo accumulates in the periphery of individual fuzz fibers (i.e. the Mo signal is higher and W signal is lower in the fiber periphery, while the Mo signal is lower and W signal is higher in the fiber interior) suggesting adatom migration along the surface. The lower Mo concentration just above the W–Mo interface in figure 3(*b*) compared to the top of fuzz fibers also suggests no pinning of punched dislocation loops from the Mo substrate at He bubbles near the interface.

While surface diffusion of adatoms generated by ion impact of the surface [18, 19] would lead to substrate accumulation at the fuzz tip, figure 3(*b*) shows that Mo adatoms are found at the fuzz tip despite the fact that the W–Mo interface (i.e. the white dashed line in figure 3(*b*)) lies below the surface. Hence, no ion-induced Mo adatoms are generated during plasma exposure of W–Mo 6, and conventional fuzz (as opposed to large nanostructure fiberforms [36] and nanotendril bundles [37, 38]) may form without ion-induced adatoms. Similarly, viscoelastic flow of material around He bubbles within fuzz fibers and at the fuzz base [20] would also lead to substrate accumulation at the fuzz surface. However, fuzz growth by viscoelastic flow would occur at a much slower rate than fuzz growth by diffusion of interstitial loops and adatoms. From reference [20], the diffusion of W by viscoelastic flow is assumed to be equal to the fuzz growth rate, which is 6.6 × 10^{-16} m^2 s^{-1} at 1120 K [39]. In contrast, diffusion of W interstitial loops is expected to be on the order of 10^{-8} m^2 s^{-1} at 1100 K [16, 40, 41] and diffusion of W adatoms over the W surface is on the order of 10^{-11} m^2 s^{-1} at 1100 K [16, 42, 43].

At <800 K, a lack of fuzz growth and significant material transport is likely due to lower mobility of He atoms and small He clusters, and hence to a smaller growth rate of He bubbles and of interstitial dislocation loops: recall the less than 2 nm bubbles formed in W–Mo 11 at 700 K compared to the up to 45 nm bubbles in W–Mo 6 at 1000 K. However, this may

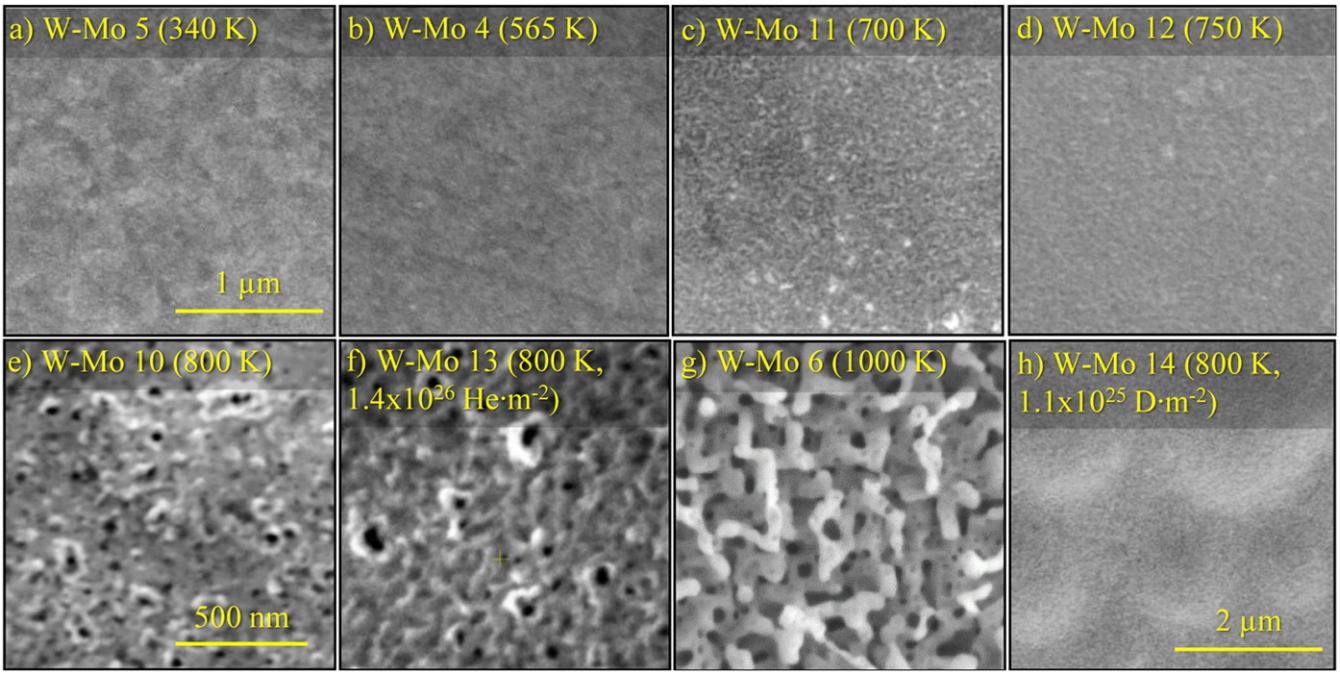

Figure 2. SEM images of the top views of W thin films on Mo substrates exposed to He plasma at ∼45 eV, 1.0–1.4 × 10^{25} He·m^{-2}, and various temperatures: (*a*) 340, (*b*) 565, (*c*) 700, (*d*) 750, (*e*) 800, and (*g*) 1000 K. Also included are images of samples exposed at 800 K to (*f*) 1.4 × 10^{26} He·m^{-2} and (*h*) 1.1 × 10^{25} D·m^{-2}. The scale for (*a*)–(*d*) is 1 μm, (*e*)–(*g*) is 500 nm, and (*h*) is 2 μm.

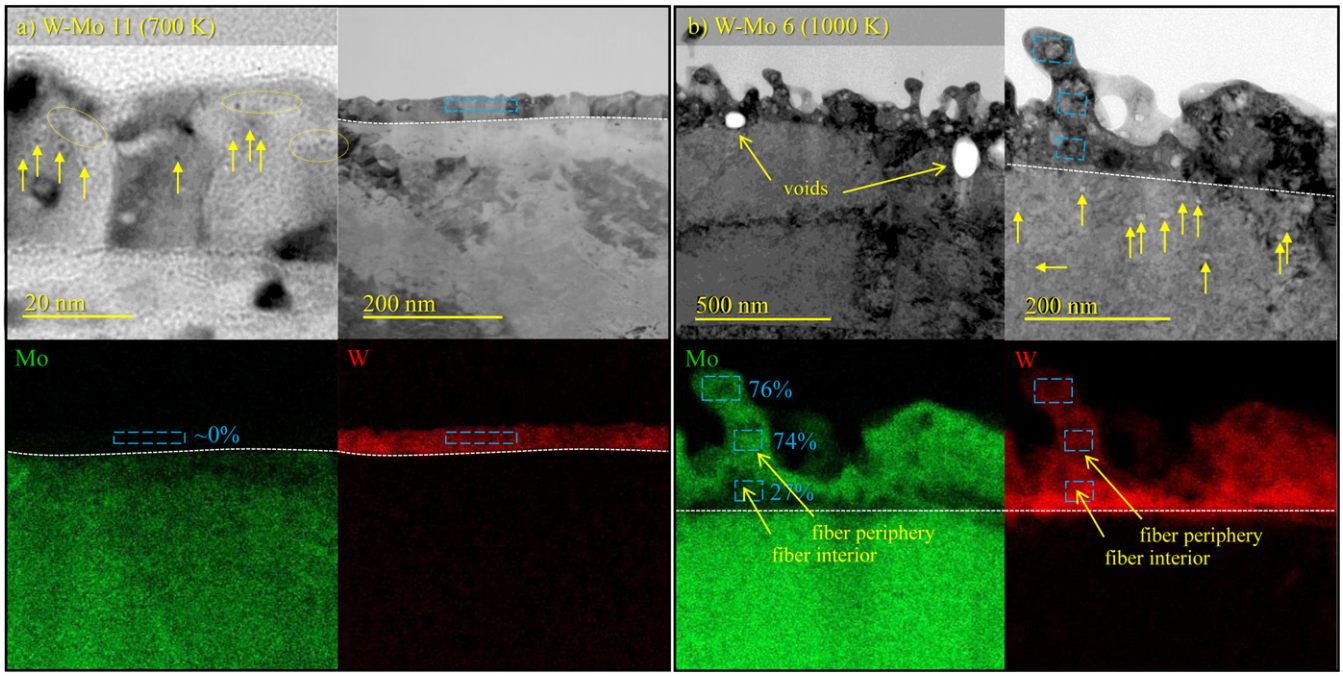

Figure 3. TEM images of He bubbles in W thin films on Mo substrates exposed to He plasma at ∼45 eV, 1.0 × 10^{25} He·m^{-2}, and (*a*) 700 or (*b*) 1000 K. Circles enclose and arrows point to He bubbles in (*a*) and (*b*), unless otherwise noted. EDX maps show Mo and W intensity in green and red, respectively. Blue boxes outline regions where Mo and W concentrations were quantified.

Table 2. Plasma exposure conditions for Mo films on W substrates. Fuzz thicknesses, L_{fuzz}, and surface concentrations of W after plasma exposure are also included. $\Phi_{He} = 3.4 \times 10^{25}$ m^{-2} for all samples.

Sample	T_s (K)	t_{film} (nm)	E_i (eV)	Γ_{He} (10^{21} m^{-2} s^{-1})	L_{fuzz} (nm)	Surface W (at%)
Mo–W 3A	838	42 ± 11	19–37	3	270 ± 40	31
Mo–W 4A	838	107 ± 14	19–37	3	460 ± 35	0
Mo 15	838	Bulk	13–37	3–4	Fuzz	n.a
Mo–W 5A	1005	77 ± 16	18–27	4–5	520 ± 65	43
Mo–W 5B	1005	135 ± 23	18–27	4–5	435 ± 60	0
Mo–W 3B	1075	64 ± 10	18–39	3–4	870 ± 60	76
Mo–W 4B	1075	133 ± 18	18–39	3–4	535 ± 100	0–10

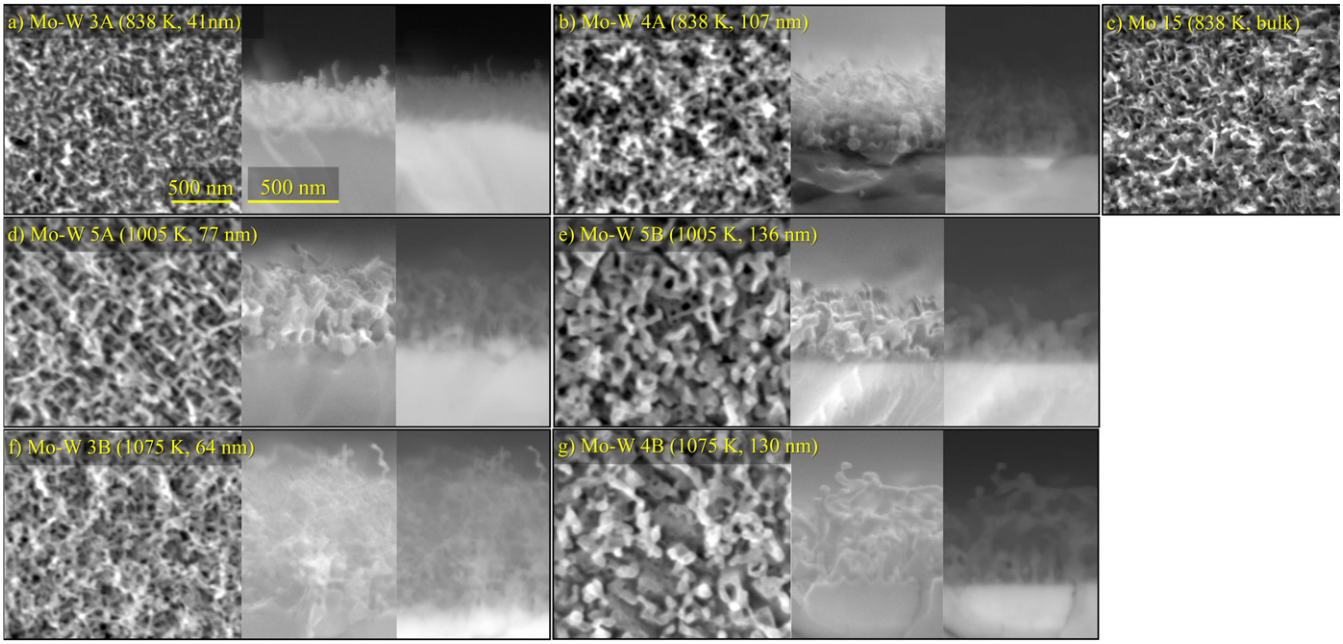

Figure 4. SEM images of the top and cross-sectional views of samples exposed to mixed D–He plasma at <40 eV, 3.4×10^{25} He·m^{-2}, and (*a*)–(*c*) 838, (*d*) and (*e*) 1005, or (*f*) and (*g*) 1075 K. Mo film thicknesses for samples in (*a*), (*d*), (*f*) are 41–77 nm and samples in (*b*), (*e*), (*g*) are 107–135 nm, while (*c*) is a bulk Mo sample. Cross-sectional images were obtained with a (left) secondary electron and (right) backscattered electron detector. Note that the scale bar for top views is slightly different than that for cross-section images, but are the same across all samples and are shown in (*a*). Images in (*a*), (*d*), and (*f*) are reproduced from [23].

also be due to smaller rates for diffusion of interstitial loops in the bulk and surface diffusion of adatoms at these lower temperatures.

3. Film thickness dependence (Mo film on W)

The dependence of bubble and fuzz formation on the film thickness was examined with samples of 42–135 nm Mo films deposited on W substrates, in addition to a bulk Mo sample. Samples were exposed at $\Gamma_{He} = 3$–5×10^{21} m^{-2} s^{-1}, $\Phi_{He} = 3.4 \times 10^{25}$ m^{-2}, and $T_s = 838$, 1005, or 1075 K. To avoid sputtering of Mo by He^+, E_i was minimized by electrically floating the samples, resulting in $E_i < 40$ eV. However, to avoid the possibility of carbon and oxygen accumulation on the sample surface, deuterium (D) was mixed into the He plasma (i.e. He comprised ~20% of the total ion flux as determined spectroscopically [44], $\Gamma_{He} \approx 0.2 \times \Gamma_i$). It should be noted that the floating potential of the sample became deeper, i.e. E_i became larger, as fuzz grew up, because of the reduced secondary electron emission [26, 45]. Plasma exposure conditions for samples used to study the film thickness, t_{film}, dependence are summarized in table 2.

Samples were analyzed after exposure with SEM, TEM, EDX, and AES as described in section 2. In addition, cross-sectional views of the samples were obtained with secondary and backscattering electron detectors on the SEM after fracturing the samples in half. Fuzz thicknesses, L_{fuzz}, were measured from cross-sectional SEM images with secondary electron detector. The backscattering detector allowed insight into the elemental composition with nm-lateral resolution, since the backscattering yields from heavier W ($Z = 74$) and lighter Mo ($Z = 42$) are significantly different. As mentioned in section 1, results from Mo–W samples 3A, 5A, and 3B were previously published in reference [23] and are summarized here for better comparison of the thinner-film and thicker-film samples.

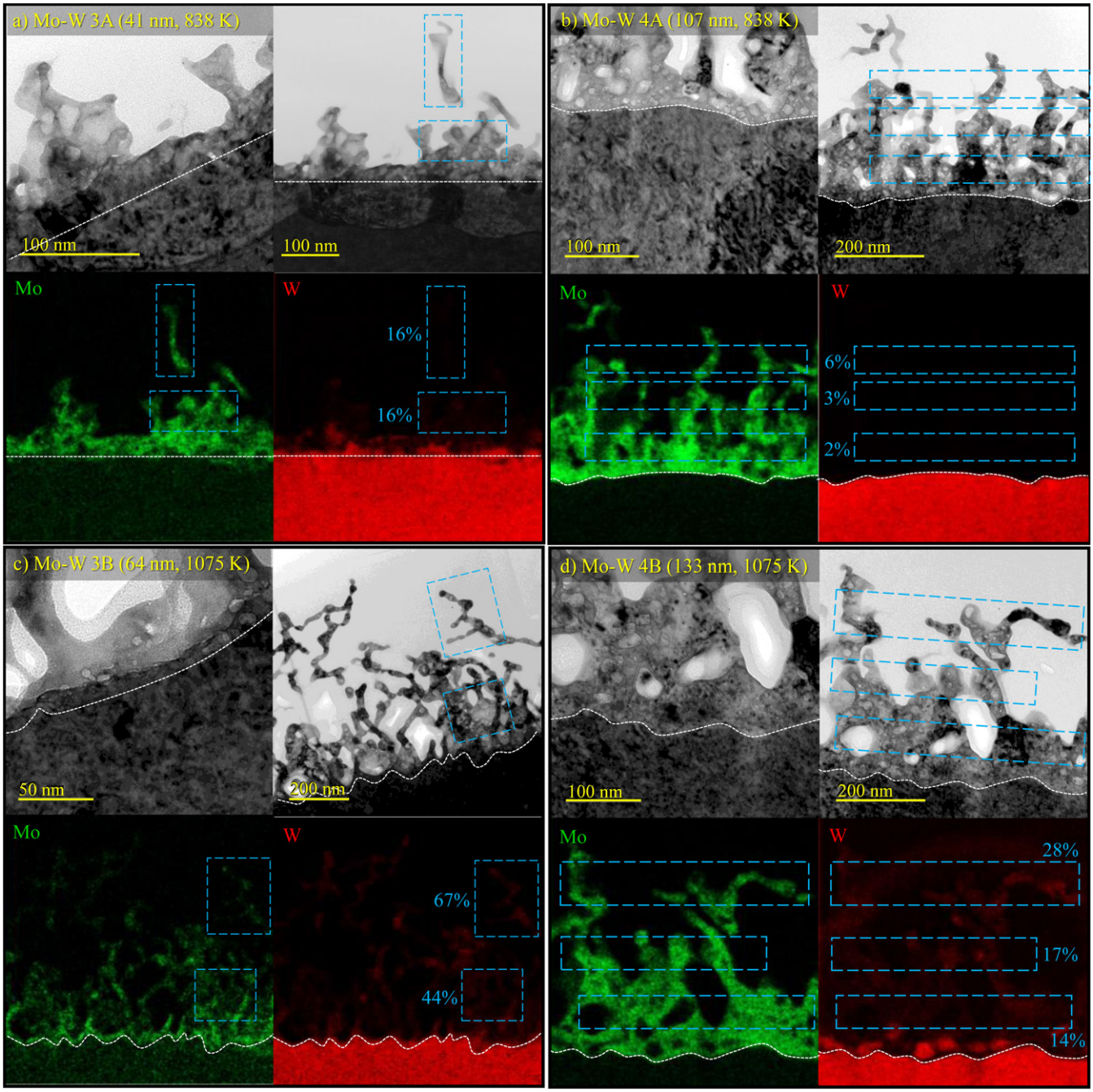

Figure 5. TEM images of He bubbles in thin Mo films on W substrates exposed to mixed D–He plasma at <40 eV, 3.4×10^{25} He·m^{-2}: (*a*) 41 nm film and 838 K, (*b*) 107 nm film and 838 K, (*c*) 64 nm film and 1075 K, and (*d*) 133 nm film and 1075 K. EDX maps show Mo and W intensity in green and red, respectively. Blue boxes outline regions where Mo and W concentrations were quantified. Images in (*a*) and (*c*) are reproduced from [23].

SEM images of the Mo thin film and bulk samples are found in figure 4. In addition, TEM images of the thin film samples are found in figure 5. All samples developed fuzz after plasma exposure. In particular, figure 4(*c*) demonstrates that fuzz forms on pure Mo at $\Phi_{He} = 3.4 \times 10^{25}$ m^{-2} and T_s down to 838 K, in agreement with reference [28], and initiated at ion energies as low as 13 eV.

As was the case for the W–Mo samples, the bubble diameter and fuzz thickness for the thin 41–77 nm Mo–W samples increase with increasing T_s due to increased mobility and coalescence of He atoms and small He clusters [46, 47], increased diffusion of interstitial dislocation loops in the bulk [16, 40, 41], and increased diffusion of adatoms on the surface [16, 42, 43]: up to 2 and 25 nm-diameter bubbles are observed in the overlayer at 838 and 1075 K, respectively, in figure 5, while 270, 520, and 870 nm thick fuzz developed at 838, 1005, and 1075 K, respectively, from figure 4. The W transport to the surface also increases with increasing T_s: 31, 43, and 76% W were measured at 838, 1005, and 1075 K, respectively, by AES (see figure 6(*a*)). At 1075 K, Mo–W 3B shows a larger

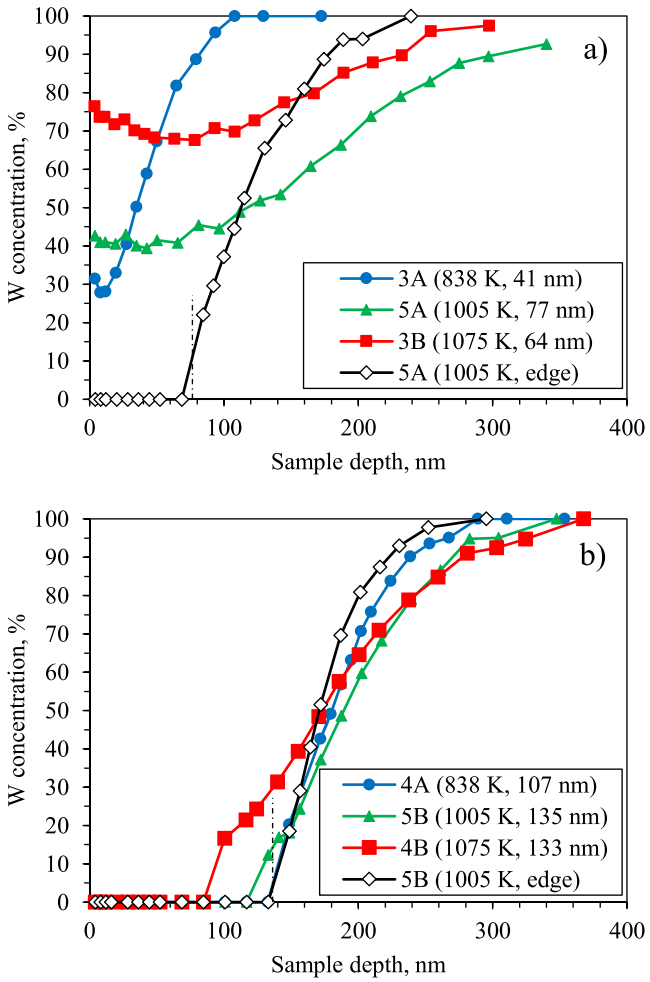

Figure 6. Concentration of W as a function of depth for (*a*) 41–77 nm and (*b*) 107–135 nm Mo films on W substrates after exposure to mixed D–He plasma at <40 eV, 3.4×10^{25} He·m^{-2}, and 838–1075 K. Profiles are also plotted for the edge which underwent thermal loading but no He plasma (dashed line indicates pre-exposure film thickness). The plot in (*a*) is reproduced from [23]. © 2020 The Royal Swedish Academy of Sciences. All rights reserved. (Note that the sample depth calibration does not consider differences in sputtering rate and AES information depth for fuzzy samples).

accumulation of W material from the substrate at the fuzz surface compared to deeper in the fuzz: 76 and 68% W was measured at ∼0 and ∼80 nm from the surface by AES. Higher fractions of W at the fuzz surface was also observed by EDX. Therefore, the substrate accumulation at the fuzz surface occurs for both W–Mo and Mo–W samples and is independent of materials chosen for the film and substrate.

W surface concentrations from AES and near-surface concentrations from EDX are plotted as a function of Mo film thickness t_{film} in figure 7(*a*) and show less material mixing for the 107–135 nm samples when compared to the 41–77 nm samples. This is also demonstrated in the full AES depth profiles in figure 6, where steeper slopes are observed near the interface, and in the cross-sectional images in figure 4, where a clearer interface is seen in the cross-sectional backscattering image of the thicker-film samples but not thinner-film samples. For samples with thicker Mo films, fuzz must grow beyond a certain thickness such that the bubble layer reaches the Mo–W interface. Hence the interface is reached at a larger fluence for thicker Mo films, resulting in less time for material mixing.

Maximum bubble diameters estimated from the TEM images in figure 5 are plotted as a function of t_{film} in figure 7(*b*). Bubbles in the fibers and at the fuzz base increase in size with increasing t_{film}. This is likely due to the fact that fuzz from samples with thicker Mo films have larger concentrations of Mo (i.e. less %W). The shear modulus of Mo is lower than that of W, hence the He pressure threshold for trap mutation and dislocation loop punching are reduced for Mo [48–50], resulting in facilitated bubble size growth by trap mutation and bubbles that are expected to be larger in Mo. While He diffusion and coalescence plays an important role in bubble growth, it cannot explain the larger bubble diameters observed for increasing Mo concentration. The He atom diffusivity is ∼2.5x higher in Mo than W at these temperatures [51], but the binding energies for He clusters and He-vacancy complexes is larger in W than Mo [51–55] (indicating that He more easily agglomerates in W than Mo with or without a vacancy). Furthermore, niobium forms fuzz with larger fiber diameters (and hence likely larger bubbles) than Mo [53] despite larger He atom diffusivity [51, 56, 57] and larger He cluster binding energy in Mo [52, 53]; the larger fiber diameters in niobium can be explained by the lower shear modulus for niobium compared to Mo [58, 59].

Fuzz thicknesses estimated from figures 4 and 5 are plotted in figure 7(*c*) as a function of t_{film}. At 838 K, L_{fuzz} increases with t_{film} since at 838 K pure Mo develops fuzz while pure W does not [6, 28], but W is still incorporated in fuzz in the mixed Mo–W material. The concurrent increase in the bubble diameter and L_{fuzz} suggests that the rate of fuzz growth is limited by the rate of trap mutation and dislocation loop punching (which are expected to be larger in Mo than W) at this temperature. At 1075 K (i.e. T_s at which both pure Mo and pure W develop fuzz), L_{fuzz} decreases and individual fuzz fibers are coarser with increasing Mo film thickness, as shown in figure 4. Larger fiber diameters in pure Mo than in pure W at ∼1000 K were observed by reference [28, 60] and as mentioned previously may be due to the lower shear modulus, facilitated trap mutation, and larger bubble diameters for Mo. The fiber diameter is expected to be influenced by the diameter of bubbles in the bulk since dislocations loops are punched when their size approaches the size of the He bubble [48], the dislocation loops glide to the surface to form adatoms islands which may be the same size as the dislocation loop (i.e. for (111) grains), and successive adatom islands may stack to form fuzz fibers [61]; the size and density of bubbles intersecting the surface during initial fuzz growth affects the size and density of pinholes formed, and hence may also affect the interfiber spacing and fiber diameter. Hence, this may explain the coarser fuzz with larger fiber diameters observed in thicker Mo films (i.e. larger concentration of Mo). The decrease in L_{fuzz} (yet increase in the bubble diameter) with increasing t_{film} at 1075 K suggests that the addition of W in thinner film samples may facilitate other steps in the fuzz formation process. Surface diffusion of

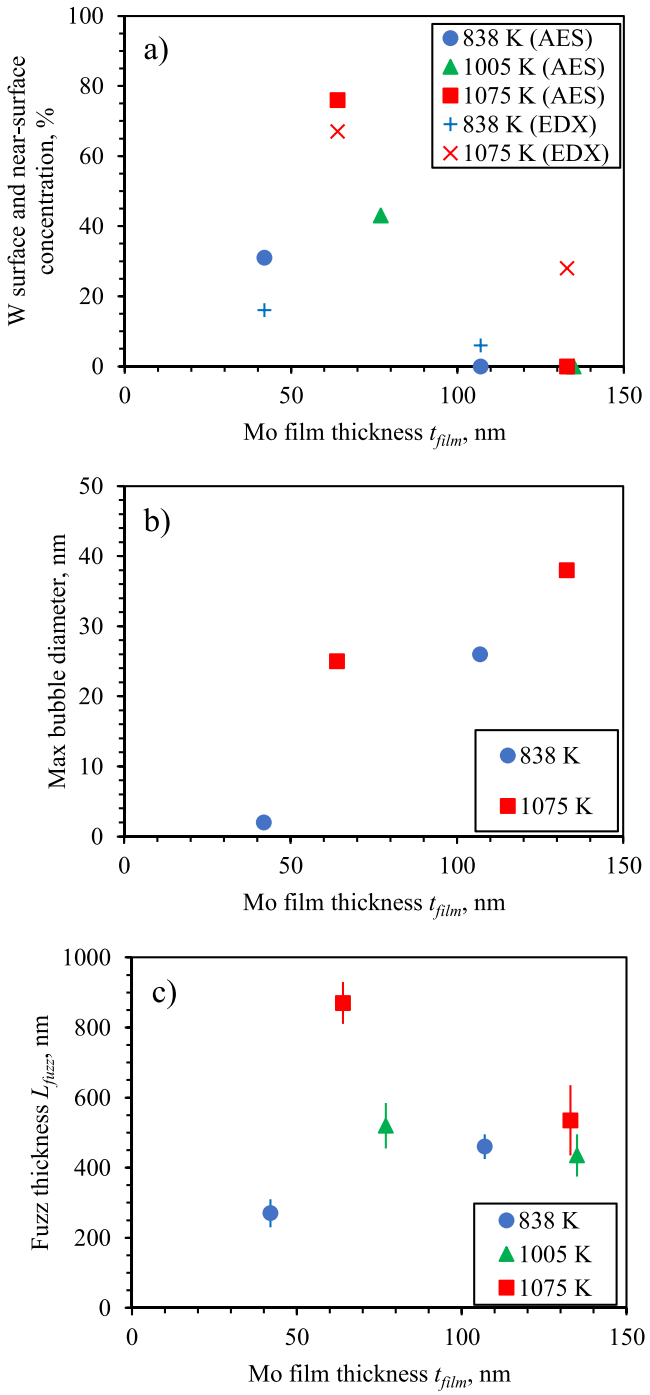

Figure 7. (*a*) W surface concentration from AES and near-surface concentration from EDX, (*b*) max bubble diameter, and (*c*) fuzz thickness as a function of Mo film thickness t_{film} for samples exposed to mixed D–He plasma at <40 eV, 3.4×10^{25} He·m^{-2}, and 838–1075 K.

adatoms is faster for Mo on Mo than W on W at these high temperatures (e.g. ~100x higher at 1800 K [43, 62]). Yet, assuming diffusion of ⟨111⟩ dumbbell self-interstitials is indicative of the relative diffusion of interstitial dislocation loops, faster diffusion of dislocation loops is expected for W than Mo [63]. Larger L_{fuzz} in pure W versus pure Mo was previously observed at 1473 K, 45 eV, $3–4.5 \times 10^{26}$ m^{-2} [60]. At 1005 K, L_{fuzz} is approximately the same for 77 and 135 nm samples due maybe to these competing effects: larger trap mutation and dislocation loop punching in Mo versus larger diffusion of interstitial loops in W.

4. Summary and conclusion

The growth of He-induced bubbles and fuzz in the near-surface region of W and Mo were investigated for T_s between 340–1075 K, Φ_{He} between $1.0–14 \times 10^{25}$ m^{-2}, and $E_i < 50$ eV. Thin 35–135 nm films on bulk substrates (i.e. W on Mo and Mo on W) were used to track material transport during bubble and fuzz growth.

At $\leqslant$750 K (i.e. conditions at which no fuzz develops in pure W and pure Mo), no fuzz and no material mixing occurred, despite the existence of up to 2 nm-diameter bubbles in the film. At 800 K (i.e. T_s at which fuzz develops in pure Mo but not in pure W), pinholes—precursors of fuzz formation—and material mixing with both Mo and W in the nanostructures are observed. Hence, fuzz forms in mixed materials if the conditions for fuzz formation in one material is met, yet the other materials may still be incorporated in the fuzz. At $\geqslant$1000 K (i.e. T_s at which fuzz develops in both pure W and pure Mo), larger bubbles, further-developed fuzz, and larger material mixing are observed. Accumulation of substrate material at the fuzz surface of thin-film samples suggests that fuzz grows by material transport from the bubble layer in the bulk to the fiber tips by diffusion of punched dislocation loops in the bulk toward the fuzz base followed by diffusion of adatoms along the fuzz base and fiber surface, with effective transport of adatoms upwards due to trapping of adatoms at curved fiber tips and/or due to a gradient in adatom concentration along the length of fibers. Other processes for *continuous* fuzz growth were ruled out, since those would not reproduce the substrate accumulation at the fuzz surface (i.e. creation of trenches by bubbles intersecting the surface at the base, or formation and fracturing of material loops by bubble-induced stress), would occur at a much slower rate (i.e. material transport by viscoelastic forces), or were dismissed in previous experiments (i.e. material transport by the sheath electric field); He bubbles intersecting the surface, however, lead to pinholes and contribute to *initial* nanostructuring.

W from the substrate integrated into the fuzz decreases with increasing Mo film thickness due to larger He fluence required for the bubble layer to reach the Mo–W interface. Since trap mutation and dislocation loop punching are expected to occur at lower He pressure threshold conditions in pure Mo than pure W (due to lower shear modulus of Mo), it is expected that He bubbles in pure Mo are generally larger than those in pure W, resulting in larger bubbles in the mixed materials observed here as the Mo film thickness increases. While fuzz thickness also increases with increasing film thickness for 838 K exposures, fuzz thickness decreases with increasing film thickness at 1075 K, suggesting that the addition of W in thinner Mo film samples may facilitate other steps in the fuzz formation process including diffusion of interstitial loops.

Acknowledgments

This work was supported by the U.S. Department of Energy through Grant No. DE-FG02-07ER54912, the Fusion Energy Sciences Postdoctoral Research Program (Contract No. DE-SC0014664), the NIFS Collaboration Research Program (NIFS19KEMF154), and the US-Japan Cooperation in Fusion Research and Development.

ORCID iDs

M.I. Patino https://orcid.org/0000-0002-2622-7110
D. Nishijima https://orcid.org/0000-0002-3119-4827
M. Tokitani https://orcid.org/0000-0002-3744-2481
J.H. Yu https://orcid.org/0000-0003-0833-5131

References

[1] Wright G.M., Brunner D., Baldwin M.J., Doerner R.P., Labombard B., Lipschultz B., Terry J.L. and Whyte D.G. 2012 *Nucl. Fusion* **52** 042003
[2] Doerner R.P. *et al* 2016 *Phys. Scr.* **T167** 014054
[3] Kajita S., Takamura S., Ohno N., Nishijima D., Iwakiri H. and Yoshida N. 2007 *Nucl. Fusion* **47** 1358–66
[4] Kajita S., Takamura S. and Ohno N. 2009 *Nucl. Fusion* **49** 032002
[5] Miyamoto M., Nishijima D., Ueda Y., Doerner R.P., Kurishita H., Baldwin M.J., Morito S., Ono K. and Hanna J. 2009 *Nucl. Fusion* **49** 065035
[6] Kajita S., Sakaguchi W., Ohno N., Yoshida N. and Saeki T. 2009 *Nucl. Fusion* **49** 095005
[7] Baldwin M.J., Lynch T.C., Doerner R.P. and Yu J.H. 2011 *J. Nucl. Mater.* **415** S104–7
[8] Kajita S., Yoshida N., Yoshihara R., Ohno N. and Yamagiwa M. 2011 *J. Nucl. Mater.* **418** 152–8
[9] Petty T.J., Baldwin M.J., Hasan M.I., Doerner R.P. and Bradley J.W. 2015 *Nucl. Fusion* **55** 093033
[10] Ueda Y., Coenen J.W., De Temmerman G., Doerner R.P., Linke J., Philipps V. and Tsitrone E. 2014 *Fusion Eng. Des.* **89** 901–6
[11] De Temmerman G., Hirai T. and Pitts R.A. 2018 *Plasma Phys. Control. Fusion* **60** 044018
[12] De Temmerman G., Doerner R.P. and Pitts R.A. 2019 *Nucl. Mater. Energy* **19** 255–61
[13] Wirth B.D., Hammond K.D., Krasheninnikov S.I. and Maroudas D. 2015 *J. Nucl. Mater.* **463** 30–8
[14] Bi Z. *et al* 2019 *Nucl. Fusion* **59** 086025
[15] Donnelly S.E. 1985 *Radiat. Eff.* **90** 1–47
[16] Dasgupta D., Kolasinski R.D., Friddle R.W., Du L., Maroudas D. and Wirth B.D. 2019 *Nucl. Fusion* **59** 086057
[17] Fan H. *et al* 2020 *Nucl. Fusion* **60** 046011
[18] Martynenko Y.V. and Nagel' M.Y. 2012 *Plasma Phys. Rep.* **38** 996–9
[19] Trufanov D., Marenkov E. and Krasheninnikov S. 2015 *Phys. Procedia* **71** 20–4
[20] Krasheninnikov S.I. 2011 *Phys. Scr.* **T145** 014040
[21] Karpov V.G. 2014 *Phys. Rev. Appl.* **1** 044001
[22] Fiflis P., Connolly N. and Ruzic D.N. 2016 *J. Nucl. Mater.* **482** 201–9
[23] Patino M.I., Nishijima D., Tokitani M., Nagata D. and Doerner R.P. 2020 *Phys. Scr.* **T171** 014070
[24] Goebel D.M. *et al* 1987 *J. Nucl. Mater.* **145–147** 61–70
[25] Nishijima D., Baldwin M.J., Doerner R.P. and Yu J.H. 2011 *J. Nucl. Mater.* **415** 596–9
[26] Patino M., Raitses Y. and Wirz R. 2016 *Appl. Phys. Lett.* **109** 201602
[27] Eckstein W. 2002 *Penetration (Range) IPP* Max Planck Institut für Plasmaphysik, Garching
[28] Takamura S. 2014 *Plasma Fusion Res.* **9** 1405131
[29] Nishijima D., Baldwin M.J., Doerner R.P., Tanigawa H., Wang P. and Yu J.H. 2017 *Nucl. Mater. Energy* **12** 1319–23
[30] Xu Y.-P. *et al* 2017 *Nucl. Fusion* **57** 056038
[31] Kajita S., Yoshida T., Kitaoka D., Etoh R., Yajima M., Ohno N., Yoshida H., Yoshida N. and Terao Y. 2013 *J. Appl. Phys.* **113** 134301
[32] Doerner R.P., Nishijima D., Krasheninnikov S.I., Schwarz-Selinger T. and Zach M. 2018 *Nucl. Fusion* **58** 066005
[33] Baldwin M.J. and Doerner R.P. 2010 *J. Nucl. Mater.* **404** 165–73
[34] Takamura S. and Uesugi Y. 2015 *Appl. Surf. Sci.* **356** 888–97
[35] Wang K., Doerner R.P., Baldwin M.J. and Parish C.M. 2018 *J. Nucl. Mater.* **509** 679–86
[36] Kajita S., Kawaguchi S., Ohno N. and Yoshida N. 2018 *Sci. Rep.* **8** 56
[37] Woller K.B., Whyte D.G. and Wright G.M. 2017 *Nucl. Mater. Energy* **12** 1282–7
[38] Hwangbo D., Kajita S., Ohno N., McCarthy P., Bradley J.W. and Tanaka H. 2018 *Nucl. Fusion* **58** 096022
[39] Baldwin M.J. and Doerner R.P. 2008 *Nucl. Fusion* **48** 035001
[40] Faney T. and Wirth B.D. 2014 *Modelling Simul. Mater. Sci. Eng.* **22** 065010
[41] Derlet P.M., Gilbert M.R. and Dudarev S.L. 2011 *Phys. Rev.* B **84** 134109
[42] Chen D., Hu W., Yang J., Deng H., Sun L. and Gao F. 2009 *Eur. Phys. J.* B **68** 479–85
[43] Piquet A., Roux H., Binh V.T., Uzan R. and Drechsler M. 1974 *Surf. Sci.* **44** 575–84
[44] Nishijima D., Doerner R.P., Baldwin M.J., Hollmann E.M., Seraydarian R.P. and Ueda Y. 2007 *Phys. Plasmas* **14** 103509
[45] Takamura S., Miyamoto T. and Ohno N. 2010 *Plasma Fusion Res.* **5** 039
[46] Shu X., Tao P., Li X. and Yu Y. 2013 *Nucl. Instrum. Methods Phys. Res.* B **303** 84–6
[47] Zhou Y.L., Wang J., Hou Q. and Deng H. 2014 *J. Nucl. Mater.* **446** 49–55
[48] Trinkaus H. and Wolfer W.G. 1984 *J. Nucl. Mater.* **122** 552–7
[49] Evans J.H. and Mazey D.J. 1986 *J. Nucl. Mater.* **138** 176–84
[50] Evans J.H., van Veen A. and Caspers L.M. 1981 *Scr. Metall.* **15** 323–6
[51] Samin A.J. 2020 *J. Appl. Phys.* **127** 175904
[52] Zhang P., Zou T. and Zhao J. 2015 *J. Nucl. Mater.* **467** 465–71
[53] Omori K., Ito A.M., Shiga K., Yamashita N., Ibano K., Lee H.T. and Ueda Y. 2017 *J. Appl. Phys.* **121** 155301
[54] Runevall O. and Sandberg N. 2009 *J. Phys.: Condens. Matter* **21** 335401
[55] Omori K., Ito A.M., Mun I., Yamashita N., Ibano K., Lee H.T. and Ueda Y. 2018 *Nucl. Mater. Energy* **16** 226–9
[56] Blow S. 1972 *J. Br. Nucl. Energy Soc.* **11** 371–6
[57] Remark J.F., Johnson A.B. Jr, Farrar H. and Atteridge D.G. 1976 *Nucl. Technol.* **29** 369–77
[58] Farraro R. and McLellan R.B. 1977 *Metall. Trans.* A **8** 1563–5
[59] Farraro R.J. and McLellan R.B. 1979 *Metall. Trans.* A **10** 1699–702
[60] De Temmerman G., Bystrov K., Zielinski J.J., Balden M., Matern G., Arnas C. and Marot L. 2012 *J. Vac. Sci. Technol.* A **30** 041306
[61] Sefta F., Juslin N. and Wirth B.D. 2013 *J. Appl. Phys.* **114** 243518
[62] Binh V.T., Uzan R. and Drechsler M. 1976 *Surf. Sci.* **57** 118–24
[63] Ma P.W. and Dudarev S.L. 2019 *Phys. Rev. Mater.* **3** 043606